Preprint typeset using LaTeX style emulateapj v. 14/09/00

TRACING THE MASS DURING LOW-MASS STAR FORMATION. II. MODELLING THE SUBMILLIMETER EMISSION FROM PRE-PROTOSTELLAR CORES

Neal J. Evans II[1,2]
Department of Astronomy, The University of Texas at Austin, Austin, Texas 78712–1083
nje@astro.as.utexas.edu
Jonathan M. C. Rawlings
Department of Physics and Astronomy, University College London, Gower Street, London WC1E 6BT, UK
jcr@star.ucl.ac.uk
Yancy L. Shirley
Department of Astronomy, The University of Texas at Austin, Austin, Texas 78712–1083
yshirley@astro.as.utexas.edu
Lee G. Mundy
Department of Astronomy, University of Maryland, College Park, MD
lgm@astro.umd.edu

ABSTRACT

We have modeled the emission from dust in pre-protostellar cores, including a self-consistent calculation of the temperature distribution for each input density distribution. Model density distributions include Bonnor-Ebert spheres and power laws. The Bonnor-Ebert spheres fit the data well for all three cores we have modeled. The dust temperatures decline to very low values ($T_d \sim 7$ K) in the centers of these cores, strongly affecting the dust emission. Compared to earlier models that assume constant dust temperatures, our models indicate higher central densities and smaller regions of relatively constant density. Indeed, for L1544, a power-law density distribution, similar to that of a singular, isothermal sphere, cannot be ruled out. For the three sources modeled herein, there seems to be a sequence of increasing central condensation, from L1512 to L1689B to L1544. The two denser cores, L1689B and L1544, have spectroscopic evidence for contraction, suggesting an evolutionary sequence for pre-protostellar cores.

Subject headings: stars: formation — ISM: dust, extinction — ISM: clouds — ISM: individual (L1689B, L1544, L1512)

1. INTRODUCTION

Molecular cloud cores that have not yet formed a star provide the best opportunity to determine the initial conditions for star formation. The density distribution as a function of radius in such starless cores is a strong discriminator between theoretical models, and it provides an essential tool for understanding the process of collapse and star formation that follows (André, Ward-Thompson, & Barsony 2000). However, the earliest evolution of a cloud core is very poorly constrained, and its evolutionary track is unclear.

For those more evolved objects that possess infrared sources, the sequence is well described by the empirical evolutionary sequence of Lada (1987), which is supported by theoretical modeling of the spectral energy distribution (SED) (Adams, Lada, & Shu 1987). In this scheme, the well-known classification (i.e. Class I, II and III) is based on the near-infrared spectral index and is interpreted in terms of the sources becoming progressively less embedded in circumstellar dust. The scheme was extended to younger, more deeply embedded objects with the Class 0 classification of André, Ward-Thompson, & Barsony (1993). These objects possess a highly enshrouded IRAS source (so that their SEDs peak longward of 100 μm); accretion models suggest that the mass of the central object is less than or similar to that of the collapsing envelope. Once a protostellar core has formed, the density distributions are strongly centrally peaked and the evolution of the objects has a "singular" nature in that the dynamics are primarily determined by the characteristics of the innermost regions of the cores.

At earlier stages of evolution, starless cores, defined as dense cores of gas that do not possess an IRAS source (Myers & Benson 1983; Benson & Myers 1989), are potential sites of star-formation. An important breakthrough in the study of these objects was the detection of dust continuum emission at millimeter and submillimeter wavelengths by Ward-Thompson et al. (1994), who dubbed the subset of starless cores that possess such emission "pre-protostellar cores" (hereafter PPCs).

However, unlike the Class 0–III sources described above, the classification of a source as a PPC can have a much broader interpretation: the density distribution in these objects could be anything between uniform and strongly centrally peaked. They may or may not be gravitationally bound. Moreover, the dynamical and evolutionary status of PPCs is poorly defined; they may be quasi-statically contracting (perhaps supported by non-thermal pressures), or in an early stage of dynamic collapse. Alternatively, it is possible that a combination of magnetic, turbulent and other effects may inhibit collapse or even

[1] University College London, Gower Street, London WC1E 6BT, UK
[2] Leiden Observatory, P. O. Box 9513, 2300 RA Leiden, the Netherlands

suppress it completely.

It is crucially important to establish the physical conditions within the extended envelopes of PPCs since they will determine most of the early evolutionary history of the sources as they evolve towards main-sequence stars. In particular, the initial conditions are highly important in defining the collapse dynamics, the likely mass of the star (and globally, the initial mass function), the timescales for evolution, and the likelihood of detection of sources in different evolutionary epochs.

Different initial conditions lead to very different collapse dynamics. Collapse from a singular isothermal sphere leads to the "inside-out" collapse model with a constant mass accretion rate (Shu 1977). If collapse begins before the density distribution relaxes fully to a singular isothermal sphere, there will be an initial period of much higher mass accretion rate, followed by a declining rate of accretion (Foster & Chevalier 1993; Henriksen, André, & Bontemps 1997). Such an epoch has been identified with the Class 0 objects (André, Ward-Thompson, & Barsony 2000). Collapse from a logatropic sphere, which produces mass accretion rates that *increase* with time, has also been suggested (McLaughlin & Pudritz 1997). To address these issues, it is necessary to understand the density and temperature distributions within the cores and to correlate them to the kinematics. In this paper we address the first of these issues.

In the original studies of PPCs (Ward-Thompson et al. 1994; Ward-Thompson, Motte, & André 1999), the radial distribution of the continuum emission was found to be relatively flat toward the center of the PPCs; this *intensity* distribution was interpreted purely in terms of a *density* distribution that is relatively flat within the inner core and falls off as an approximate power law at larger separations. These authors, and others, have invoked such density distributions as proof of the significance of non-thermal (magnetic and/or turbulent) pressure support in these objects. However, Ward-Thompson, Motte, & André (1999) pointed out that the source statistics and, where available, the observed magnetic field strengths suggest a quantitative disagreement with the evolutionary timescales in the published ambipolar diffusion models for the quasi-static contraction of magnetized cloud cores. This conclusion has been questioned by Ciolek & Basu (2001).

These conclusions are important in constraining the collapse process, but previous interpretations of the data assumed that the dust temperature is uniform throughout the cores. We will argue that the interpretations of the observational data are profoundly affected by this assumption. Early calculations for dust clouds heated by the external radiation field found that the temperature declined to very low values in the interior (Leung 1975); more recently Zucconi et al. (2001) have applied a semi-analytic technique and come to similar conclusions.

In this paper, we constrain the density and temperature profiles of a small sample of PPCs, utilizing high quality observational data and a dust continuum radiative transfer code (Egan, Leung, & Spagna 1988). We consider a range of physical models for the density distribution, calculating the dust temperature distribution in each case in a self-consistent way. The model clouds are then "observed" to mimic the observational technique (including the effects of the telescope beam power pattern and chopping) in order to compare to actual observations. Although several sources of observational data are considered, the primary observational comparison is to our recent 450μm and 850μm data obtained with the SCUBA on the James Clerk Maxwell Telescope (JCMT) (Shirley et al. 2000).

2. PHYSICAL MODELS

We consider the simplest physical situation of thermally supported, gravitationally bound, spherically symmetric clouds. While all three cores modeled here have some degree of turbulence, it is subsonic in L1512 and L1544 or barely sonic in L1689B; the effects of turbulence should not be dramatic in these very quiescent cores. The solution for the thermally-supported, isothermal cloud is the Bonnor-Ebert sphere, which can be generalized to account for a temperature gradient (see below). In addition to the thermally supported Bonnor-Ebert spheres, we have also considered a singular sphere, for which $\rho \propto r^{-2}$, normalized to match a Bonnor-Ebert model at the outer radius. Magnetically supported cores have also been suggested (Ciolek & Mouschovias 1994; Ciolek & Basu 2000). The latter authors have presented density profiles that are specifically appropriate to L1544. Although a comparison with these models would be of great interest, the inclusion of magnetic pressures necessarily implies significant deviations from spherical symmetry – in fact, highly flattened disk-like structures are predicted. After some attempts to capture the essence of these models in the one dimensional models we consider here, it became clear that a fully two dimensional treatment is required. We defer discussion of these magnetic models to future work but discuss the possible effects of asphericity on our modeling in §8.

We have considered two types of hydrostatic pressure-balanced cloud:

1. "Classical" isothermal Bonnor-Ebert spheres, in which $(dT/dr) = 0$; and
2. Modified Bonner-Ebert spheres with a gradient in the kinetic temperature.

If the gravitationally bound clouds are non-magnetic, are not subject to any large-scale systemic velocity flows (rotation, infall, or outflow), and are purely supported by thermal pressure, then the equations of hydrostatic equilibrium are as follows:

$$\frac{dP(r)}{dr} = -\frac{GM(r)\rho(r)}{r^2}, \tag{1}$$

$$\frac{dM(r)}{dr} = 4\pi r^2 \rho(r), \tag{2}$$

where r is the radius, $P(r)$ and $\rho(r)$ are the pressure and density respectively at r, and $M(r)$ is the total mass enclosed within r. If the clouds are isothermal, the equation of state is

$$P = a^2 \rho, \tag{3}$$

where a is the isothermal sound speed ($a^2 = kT/\mu m_H$, k is the Boltzmann constant, μ is the average molecular mass in the gas, and m_H is the mass of the hydrogen atom).

With an appropriate change of variables to a dimensionless form, $D = \rho/\rho_c$ and $\xi = (r/a)\sqrt{4\pi G\rho_c}$, where ρ_c

is the central density, these equations yield a single solution, with the maximum value of ξ ($\xi_{max.}$) as the only free parameter (cf. Foster & Chevalier, 1993), which is determined by pressure balance with the surrounding medium. If $\xi_{max.} > 6.451$, which corresponds to a center-to-edge density contrast of $\rho_0/\rho_c > 14.3$, then the sphere is unstable to perturbations and subsequent gravitational collapse. The marginal case is the "critical Bonnor-Ebert sphere" (Ebert 1955, Bonnor 1956). The solution corresponds to a family of spheres of differing central density [cf. Fig. 1 of Shu (1977)]. The density structure of the outer envelopes is closely approximated by $\rho \propto r^{-2}$, but the density approaches a constant value at small r. For a given temperature, higher values of ρ_c yield models with smaller cores. The most extreme form of the unstable Bonnor-Ebert sphere has an infinite central density (corresponding to $\xi_{max.} = \infty$). This is the singular isothermal sphere, in which $\rho \propto r^{-2}$ throughout.

The modified Bonnor-Ebert spheres include the effects of radial temperature variations. In these cases,

$$\frac{dP}{dr} = k\left[n\frac{dT}{dr} + T\frac{dn}{dr}\right], \tag{4}$$

and, using $\rho = \mu m_H n$, where n is the number density, equation 2 becomes

$$\frac{dM(r)}{dr} = (4\pi\mu m_H) n r^2 \tag{5}$$

and, from hydrostatic equilibrium,

$$\frac{dn}{dr} = -\left(\frac{\mu m_H G}{k}\right)\frac{M(r)n}{Tr^2} - \left(\frac{n}{T}\right)\frac{dT}{dr}. \tag{6}$$

In all of our models the mean molecular mass is $\mu = 2.3$, consistent with $n = n(\mathrm{H_2}) + n(\mathrm{He})$. The inner radius ($r_i$) is not constrained by observations and is simply set small enough (25 AU) that it does not affect the results, as shown by tests that used $r_i = 50$ AU. The free parameters in the isothermal Bonnor-Ebert models are thus the central density (n_c), the outer radius (r_o) and the gas kinetic temperature (T_K). Most models have an outer radius of 3×10^4 AU, but some have an r_o of 1.5×10^4 or 6×10^4 AU.

For most of our models (see Table 1) we have used the isothermal Bonnor-Ebert configurations with $T_K = 10$ K. The density distribution from a sequence of these models (with different central densities, n_c) is shown in Figure 1a. A few isothermal models were computed for different values of T_K to examine the sensitivity of the density structure to the temperature (Fig. 1b). The main effect of changing the assumed T_K is to change the size of the central core and the mass (Table 1).

For all cases with $n_c \geq 3 \times 10^4$ cm^{-3}, the density contrast between the edge and the center of the cores exceeds 14.3, implying that they are unstable to collapse. For the isothermal Bonnor-Ebert spheres of fixed temperature and outer radius, the enclosed mass is only slightly sensitive to the central density (n_c). Since the photometric fluxes are largely determined by the masses within the beams, observations of the spectral energy distribution (SED) alone cannot place very strong constraints on the central densities of Bonnor-Ebert spheres. However, by modeling the radial intensity distribution it is possible to discriminate between models with different central densities, which have different density *distributions*.

In order to generate the non-isothermal Bonnor-Ebert spheres it is necessary to pre-define the temperature profile. In practice, this is achieved by using an appropriately defined isothermal Bonnor-Ebert model as the input for the radiative transfer code to generate the dust temperature profile (see §3). This $T_d(r)$ is then used to recalculate the density profiles in the non-isothermal model. Obviously, the corrected density profile could then be used to generate a second iteration for the temperature profile etc., but the magnitude of the corrections in the second and higher order iterations is sufficiently small for them to be neglected. The correction for non-isothermality results in a smaller core and an initially steeper density profile (Fig. 1c), caused by the second term in equation 6, with $dT/dr > 0$. Beyond radii of about 5000 AU, the first term in equation 6 dominates, and the smaller enclosed mass (caused by the smaller core) leads to a shallower density profile. The *total* mass is larger because the mass is dominated by the outer regions. The shallower density profile in the outer envelope decreases the center to edge density contrast (e.g. in the case of $n_c = 10^6$ cm^{-3}, $r_o = 3 \times 10^4$ AU, by a factor of $\sim$1.8).

Note that the radiative transfer code computes the radial profile of the *dust* temperature, $T_d(r)$, whereas the equilibrium configuration is determined by the *gas* kinetic temperature, $T_K(r)$. While efficient gas-dust coupling forces T_K to equal T_d at high densities, at densities below about 1×10^4 to 3×10^4 cm^{-3}, $T_K \neq T_d$ (Takahashi, Silk, & Hollenbach 1983; Doty & Neufeld 1997). Although these models are a theoretical improvement on the isothermal Bonnor-Ebert sphere, a full calculation of the gas energetics, including dust coupling, would be needed to make fully self-consistent models.

All the models of the density profiles are tabulated in Table 1. All densities are specified as the number density of particles. The notation tBE implies a non-isothermal Bonnor-Ebert model in which the density structure was computed assuming that $T_K(r) = T_d(r)$, where $T_d(r)$ was computed from the initial isothermal BE model with the same n_c (model number denoted by the superscript). We again emphasize the distinction between T_K and T_d by using the term isothermal only to refer to the assumption about $T_K(r)$ used to compute the density distribution. The *dust* temperature in these isothermal BE models is *not* constant (§3).

3. INTERSTELLAR RADIATION FIELD

The radiative transport code of Egan, Leung, & Spagna (1988), modified to use an arbitrary density distribution, computed $T_d(r)$ for each physical model. We first explored the dependence of the temperature profiles on the assumed form of the interstellar radiation field (ISRF). Figure 2 shows a comparison of two estimates of the ISRF. Previous calculations with the radiative transfer code (e.g., Leung (1975); Zhou et al. (1990)) have used an ISRF similar to that of Mathis, Mezger, & Panagia (1983), supplemented by a blackbody for the cosmic background radiation (hereafter "MMP"). More recent analyses, using the COBE data, indicate a stronger ISRF in the infrared (Black 1994). Significant departures from the "MMP" ISRF occur between 5 and 400 μm. We have modified the Black (1994) ISRF at the shorter ultravi-

olet wavelengths ($\lambda < 0.36$ μm) using equations given by van Dishoeck (1988), which reproduce the ISRF of Draine (1978). The differences between the "MMP" and the Black-Draine models of the ISRF are quite substantial, reaching a factor of 1.8 in parts of the ultraviolet, and a factor of 13 in parts of the infrared.

Figure 3 compares temperature profiles using the two different models of the ISRF, with the same physical model: a Bonnor-Ebert sphere with a central density of 1×10^6 cm^{-3} and uniform kinetic temperature, $T_K = 10$ K. The differences in $T_d(r)$ are small (≤ 1.2 K), but the biggest differences are at the cold center of the cloud, where a small change in T_d can potentially have a major impact on the emission. Comparison of the emitted fluxes calculated for different wavelengths and beams indicate modest changes (less than 15%) for $\lambda > 170$ μm, but bigger changes at shorter wavelengths. In our modeling, we use the Black-Draine model as the standard representation of the ISRF.

4. DUST OPACITIES

Dust opacities in molecular clouds clearly differ from those in the general interstellar medium. Observations of regions forming massive stars (van der Tak et al. 1999, 2000) have been well-matched by a set of opacities calculated for grains that have grown by coagulation and accretion of thin ice mantles for 10^5 years at a density of 10^6 cm^{-3}, listed in column 5 of Ossenkopf & Henning (1994) (hereafter OH5). This model of the dust opacity is therefore probably appropriate to the cold, quiescent cloud cores that are the subject of this study. We adopt these opacities as the standard model and explore the effect of using different opacities. As discussed below, the excellent agreement between the observational data and our physical models strongly supports the validity of these opacity laws.

As a specific alternative to OH5, we consider the opacities in column 2 of Ossenkopf & Henning (1994) (hereafter OH2), which include coagulation but lack ice mantles. These may be more appropriate in regions where young stars have heated the grains enough to remove the mantles. The model opacities are larger at 1300 μm than in the OH5 grain models by a factor of about 2.2 (Fig. 2). Both the OH5 and the OH2 dust models result in considerably higher opacities at long wavelengths (by a factor of 6.4 for OH2 at 1300 μm) than for models in which the grains have not undergone coagulation (e.g., column 1 of Ossenkopf & Henning (1994).

However, despite these differences, we find that the effect of the opacity law on $T_d(r)$ is small; the largest difference is at the inner radius, where OH2 opacities give a T_d that is lower by 0.5 K than that obtained with the OH5 opacity model.

5. ALTERNATIVE HEATING MECHANISMS

Because the very low temperatures of the dust grains in the centers of dense cores have a major impact on the interpretation of the submillimeter emission (§6 to §7), it is important to consider all other possible heating mechanisms in addition to the absorption of the ambient ISRF. The primary source of energy deep inside opaque cloud cores is provided by cosmic rays. We consider direct deposition of energy in dust grains by cosmic rays, absorption of ultraviolet photons produced by secondary cosmic ray excitation of H_2 molecules, and, finally, energy transfer from possibly warmer gas heated by the cosmic rays. For the purpose of a comparative study, we consider a representative grain of radius 0.1 μm, absorption properties given by OH5 dust, and a cosmic ray ionization rate $\zeta = 1 \times 10^{-16}$ s^{-1}. This value is near the maximum found in recent investigations (de Boisanger, Helmich, & van Dishoeck 1996; Caselli et al. 1998). The most recent estimates indicate $\zeta = (2.6 \pm 1.8) \times 10^{-17}$ s^{-1}, based on modeling of $H^{13}CO^+$ observations (van der Tak & van Dishoeck 2000), which is in good agreement with direct measurements by the Voyager and Pioneer spacecraft (Webber 1998). Consequently, the value that we have adopted should provide a strong upper limit to the cosmic ray heating. In each case, we compare the heat input to a grain to the radiative cooling by a grain at a temperature of 5 K, somewhat lower than the value of T_d reached at the center of the cores. Because the dust in the code is in radiative equilibrium, the cooling rate sets a lower limit on the heating rate due to the ISRF. At this temperature the power emitted by our representative grain, obtained by integrating over the product of the Planck function and the emission cross section for OH5 dust, is 4.0×10^{-15} erg s^{-1}.

Firstly, we consider the direct cosmic ray heating of dust particles. As discussed by Greenberg (1991), the energy input is maximized if we assume that all cosmic ray ionizations are caused by 1 MeV protons. Then, our value of ζ implies a flux of protons of 4.8 cm^{-2}s^{-1}, each of which can deposit 6.13 keV in the representative grain described above (Greenberg 1991). This results in an energy deposition rate per grain of 2.1×10^{-17} erg s^{-1}, 190 times smaller than the radiative heating.

Secondly, we consider the effect of ultraviolet photons created following the cosmic ray ionization of H_2. This process yields energetic electrons that are capable of collisionally exciting electronic states of H_2, which decay producing a spectrum of ultraviolet photons (Prasad & Tarafdar 1983). Estimates of the flux of these photons range from 1.4×10^3 (Prasad & Tarafdar 1983) to 1×10^4 cm^{-2}s^{-1} (Greenberg & Li 1996). A calculation of particular relevance is that of Cecchi-Pestellini & Aiello (1992), who include the effects of a density gradient and internal extinction of the photons. They consider a centrally condensed cloud with properties similar to those that we infer for pre-protostellar cores and find a maximum photon flux near the center of of $\Phi_\nu = 1 \times 10^4$ photons cm^{-2} s^{-1}, for $\zeta = 4 \times 10^{-17}$ s^{-1}. Scaling to our adopted value of ζ gives $\Phi_\nu = 2.5 \times 10^4$ photons cm^{-2} s^{-1} as a maximum value. If all of these photons are at a wavelength of 120 nm [this probably overestimates the average photon energy, (Gredel et al. 1989)], then the energy deposition per grain is

$$\Phi_\nu E_\nu Q_a \pi a^2 < 2.5 \times 10^4 \times 1.7 \times 10^{-11} \times 5.1 \times 10^{-10} = 2.2 \times 10^{-16} \text{er} \quad (7)$$

which is 18 times smaller than the heating rate due to the external ISRF.

Finally, we consider heating of dust grains by collisions with warmer gas particles. The energy deposition rate depends on the gas temperature, which is poorly constrained. However, we can put a limit to the *total* heating caused by cosmic ray heating of the gas by assuming that *all* of the

energy input to the gas is transferred to the dust. This is clearly a gross upper limit since much of the energy will be radiated away in molecular emission. The volume rate of heating by cosmic rays (Goldsmith & Langer 1978) is

$$\Gamma_{CR} = 3.2 \times 10^{-27} \Big(\frac{\zeta}{1 \times 10^{-16}} \Big) n(\mathrm{H_2}) \mathrm{erg\ cm^{-3}\ s^{-1}}, \quad (8)$$

Assuming that

$$n_d = n(\mathrm{H_2})/3.9 \times 10^{11}, \quad (9)$$

where $n(\mathrm{H_2})$ and n_d are the number densities of $\mathrm{H_2}$ molecules and dust grains, respectively, the upper limit of the heating rate per grain is 1.3×10^{-15} erg s^{-1}; still a factor of 3 less than the heating by the ISRF. In principle, we could also consider the heating of the gas by the ISRF in the outer parts of the core, but our main concern is whether or not the central regions of the cores are as cold as our models predict. In any case, the density in the outer regions is too low for the gas and dust temperatures to be well coupled. We conclude that heating by the ISRF dominates other possible heat sources for dust grains, even deep inside an opaque core.

Recent calculations of gas and dust energetics, including the effects of depletion on the coolants, support the conclusion that the gas cannot substantially raise the dust temperature (Goldsmith 2001).

6. MODELING OBSERVATIONS

The primary observational data that the models must reproduce are the radial profiles of intensity at 450 and 850 μm, as presented by Shirley et al. (2000). For some sources, intensity profiles at 1300 μm obtained with the IRAM 30-m telescope also exist. We model the radial intensity distribution, $I^{norm}(b) \equiv I_\nu(b)/I_\nu(b_0)$, as a function of impact parameter (b), normalized to the innermost impact parameter, corresponding to one quarter of the beamwidth. This measure is thus sensitive to the normalized density and temperature *distributions*, while the SED is sensitive to the ISRF and a quantity that is proportional to the product of total mass within the beam and the opacity. Thus, modeling the *normalized* radial intensity distribution and the SED separately provide roughly orthogonal constraints on different model variables. Photometric data, summarized by Shirley et al. (2000), can constrain the ISRF, mass, and model opacities. Of course, photometric data obtained with *different* beams at the same wavelength retain some sensitivity to the density and temperature distributions.

To model correctly the radial intensity distribution, one must calculate the emission from a model cloud, with a self-consistent $T_d(r)$, convolve the emission with the observed beam shape, and "chop" the model in the same way as the data were chopped during the observations. The calculation of $T_d(r)$ is done with the code of Egan, Leung, & Spagna (1988). Figure 4 shows that more centrally condensed cores (higher n_c) result in lower dust temperatures in the interior (as expected), but somewhat higher dust temperatures at larger radii until all models converge to about the same value at the edge of the cloud.

A second code then uses these density and temperature profiles [$n(r)$ and $T_d(r)$] to calculate the angular dependence of the emission at specific wavelengths, convolves with the observed beam, and uses a numerical simulation of the chopping that was used in obtaining the data to produce a predicted intensity profile, normalized in the same way as the data ($I^{norm}_{mod}(b)$). The simulation of chopping in a one dimensional code cannot replicate exactly the observations at large impact parameters. We limit our comparison of models to data to ranges of b where the predictions are insensitive to the exact model of chopping. In addition, the ratio of the normalized intensities at the two wavelengths [$I^{norm}_{450}(b)/I^{norm}_{850}(b)$] is computed to examine possible variations in the spectral index with radius. Figure 4 shows how the predicted intensity distributions are affected by the assumed form of the density distribution. Although the more condensed models lead to more rapid declines of the density with radius, beam convolution and chopping, as shown in Figure 4c and 4d, makes the difference less striking than one might expect [see also Fig. 1 of Shirley et al. (2000)].

For the 1300 μm data obtained with the 30-m IRAM telescope, the beam power pattern is available from the literature, but the data cannot be completely modeled because they were obtained with multiple chopper throws and restored. To bracket the range, we ran models with no chopping and models with a 120″ chop, based on an estimate of where the IRAM data begin to lose sensitivity (P. André, pers. comm.). Clearly, some loss of signal at large impact parameters has occurred because the unchopped models do not reproduce the declines seen in the multiply-chopped data, but chopping at 120″ may overestimate the effect.

Modeling the SED allows tests of different aspects of the models: the ISRF, the assumed dust opacities, and the mass within the beams. In particular, far-infrared data constrain the ISRF, while submillimeter data constrain the product of mass and submillimeter opacity. Photometric data are quite variable in quality; most references do not provide a beam shape and the data often represent the emission integrated over a map. In these cases, we assume a Gaussian beam. In addition, calibration uncertainties are hard to quantify. Far-infrared data from *ISO* exist (Ward-Thompson, André, & Motte 1998) and (Ward-Thompson & André 1999), but the flux density estimates were being revised to correct for background subtraction. While this paper was being refereed, the new measurements became available (Ward-Thompson et al. 2001). The new results require an ISRF lower than used in our models, but the conclusions about the best density model are unaffected. Consequently, only a few new models were calculated for each source to illustrate the effects of the lower ISRF. These new results strongly support our conclusions that the dust temperatures are very low in the centers of these cores

The agreement between the model and the data can be quantified in terms of the reduced chi-squared

$$\chi^2_r = (I^{norm}(b) - I^{norm}_{mod}(b))/\sigma)^2/N \quad (10)$$

where σ is the uncertainty in the data and N is the number of data points; only points spaced by a full beam are used in computing χ^2_r to avoid introducing correlations. Because the χ^2_r measure gives great weight to a few discrepant points and/or points with small uncertainties, we have also computed the mean absolute deviation, as used in robust estimation:

$$\langle \delta \rangle = |I^{norm}(b) - I^{norm}_{mod}(b)|/N. \quad (11)$$

The statistics were computed separately for each observation. Generally, the computations were carried out to angular distances of about 60″, beyond which inability to simulate chopping exactly make the comparison dubious for the SCUBA data. A similar calculation with the flux densities (S_ν) was used for comparing the observed and model SEDs. In Tables 2 to 4, we report the *sum* of the χ^2_r for the 450 and 850 μm data, as well as $\langle\delta\rangle$, but only χ^2_r for the comparison to 1300 μm data and the SED. The sum of χ^2_r for the SCUBA data is always dominated by the 850 μm data because of the smaller uncertainties, whereas the $\langle\delta\rangle$ weights the 450 μm and 850 μm data more equally. For the 1300 μm data, two values for χ^2_r are given in Tables 2–4, the chopped value first, and the unchopped value second. In the figures, the chopped prediction for 1300 μm is shown as a dashed line, whereas the solid line indicates unchopped models.

The χ^2_r values for the SED in most table entries do not include the new far-infrared data of Ward-Thompson et al. (2001); two models for each source, at the bottom of each table, do include these data in the χ^2_r calculation.

7. MODELLING INDIVIDUAL SOURCES

7.1. *L1689B*

For L1689B, we assume a distance of 125 pc, rather than the traditional 160 pc, based on improved determinations by de Geus, de Zeeuw, & Lub (1989), and Knude & Hog (1998), which are supported by the distance to upper Scorpius (de Zeeuw et al. 1999). The SCUBA data on this source (Shirley et al. 2000) have fairly good signal-to-noise and the source shape as projected onto the plane of the sky is reasonably circular, away from the central region. The higher contour levels are somewhat elongated and may even have weak multiple peaks. Thus, our spherical models can only be approximations to the actual source. In addition to the SCUBA data, we consider the IRAM 1300 μm map (André, Ward-Thompson, & Motte 1996). As stated above, because these data were taken with multiple chopper throws and restored, we cannot simulate the effects of chopping as we can for the SCUBA data; thus we weight the agreement with the 1300 μm data much less in deciding which models are best.

For most of the models of L1689B, whose results are summarized in Table 2, we adopt the simple, isothermal Bonnor-Ebert description of the density distribution. In these models, the primary variable is the degree of central condensation, measured by n_c. The inner radius was fixed at 25 AU, the outer radius at 3×10^4 AU, and the dust opacity was OH5. The χ^2_r and $\langle\delta\rangle$ values for the SCUBA data show a clear minimum around $n_c = 1 \times 10^6$ cm^{-3}; the 1300 μm data favor $n_c = 1 - 3 \times 10^6$ cm^{-3}. The model with $n_c = 1 \times 10^6$ cm^{-3} is a good compromise, and we adopt that value as our standard model in testing the effect of other parameters. We also explored the effects of using non-isothermal Bonnor-Ebert models, which may be a more realistic description of the density distribution. The differences in the predicted intensity distributions were very small.

The effects of chopping make the data quite insensitive to the outer radius. A model with an inner radius of 50 AU was essentially indistinguishable from the standard model, as was a model with $r_o = 6 \times 10^4$ AU. Decreasing the outer radius to 1.5×10^4 AU has very little effect on the SCUBA or 1300 μm fits.

We have also considered the effects of adopting different dust opacities. Models using OH2 dust opacities differed little from those with OH5 dust opacities in the fits to the SCUBA and the 1300 μm data, but the agreement with the SED worsened substantially. Because OH2 dust has a higher opacity at long wavelengths, these models produced too much flux. The excess flux could not be decreased by varying n_c within the range favored by the intensity profiles because the amount of mass in the beam changes little with n_c. It is remarkable in fact that OH5 dust opacity and a Bonnor-Ebert density distribution fits the SED so well. If we were sure that the cloud is hydrostatic and thermally pressure-balanced, so that a Bonnor-Ebert sphere is the correct physical model, then we could constrain the dust opacities quite strongly.

The new far-infrared data (Ward-Thompson et al. 2001) are about half the values previously reported, indicating lower T_d, and thus a lower value for the ISRF than assumed in our models. The last two models in Table 2 include these new data. The first retains the original ISRF, while the second scales the ISRF by a factor of 0.5, clearly improving the χ^2_r for the SED. The latter model is shown in Fig. 5, including the temperature profile, the 450/850 μm intensity ratio, the SED, and fits to the 450, 850, and 1300 μm normalized intensity profiles.

Given the substantial uncertainties, the model fits the data well. In particular, the data suggest (with big uncertainties) a rise in the ratio toward the edge of the cloud. The model correctly predicts this behavior which arises almost equally as a result of the increase in T_d at the edge of the cloud and as an effect of chopping. In principle, deviations of the data from the model could be used to study possible changes in dust properties with radius, but better signal-to-noise in the 450 μm data is needed before it is possible to make quantitative analyses. For the present, we note that any attempt to model the distribution of dust properties must incorporate careful considerations of spatial variations in the dust temperature and the effects of chopping. We can also compare the actual values of the spectral index α to the observations (Shirley et al. 2000). The best model produces $\alpha = 2.1$ in the 40″ beam and $\alpha = 2.4$ in the 120″ beam (see Shirley et al. (2000) for the definition of α. These values are consistent within uncertainties with the α seen in the observations (2.0 ± 0.6).

We may ask how our conclusions compare to the previous studies of André, Ward-Thompson, & Motte (1996) (AWM). Firstly, AWM assume a distance of 160 pc and an opacity at 1300 μm of $\kappa_\nu = 0.005$ cm^2 gm^{-1} of gas, whereas the corresponding value for the OH5 dust opacity is $\kappa_\nu = 0.009$ cm^2 gm^{-1} (assuming a gas to dust ratio of 100). In comparing results, we adjust the results of AWM to our assumed distance and opacity. The other main difference is that AWM assumed a constant $T_d = 18$ K, whereas we compute $T_d(r)$ and find it to be lower everywhere, especially toward the center of the cores. Because the lower T_d depresses emission from the center substantially (reducing the temperature from $T_d = 18$ K to $T_d = 7.5$ K results in a flux reduction by a factor of 4 at $\lambda = 1300\mu$m), we find higher central densities (by factors of 3–10) and a smaller radius (by factors of 0.5–0.9) for

the flattened part of the density distribution. The smallest differences are found in the model with $n_c = 3 \times 10^5$ cm^{-3}. The mass inside 10^4 AU is more similar; our mass (0.95 $M_\odot$) is 1.4 times higher than that of André, Ward-Thompson, & Motte (1996). Both studies agree that the density distribution outside the flat portion is well represented by a power law ($n(r) \propto r^{-p}$) with $p \sim 2$.

Bacmann et al. (2000) have re-analyzed the 1300 μm data, assuming a constant T_d of 12.5 K and incorporating an analysis of the absorption at $\lambda \sim 7$ μm that the cloud shows in ISOCAM data. They also find a density distribution that shows a distinction between a "flat" inner region and an envelope in which the density distribution can be described by a power law, roughly consistent with $p = 2$. They also find that Bonnor-Ebert spheres fit their data quite well. However, they find that the radius of the flat density core is 5000–6000 AU, 3 times larger than we find. This r_{flat} would correspond roughly to our Bonnor-Ebert sphere with $n_c = 1 \times 10^5$ cm^{-3}, which fits neither our SCUBA data nor the 1300 μm data, in our analysis.

In principle, the absorption method does not depend on T_d, thereby providing a complementary probe. However, the complication arises in the determination of the foreground emission, which veils the absorption by the core. Bacmann et al. (2000) use the 1300 μm data to constrain this foreground emission and conclude that the foreground is almost entirely zodiacal emission, so that the cloud must be illuminated entirely from behind. With this assumption, they find $\tau(7\mu\text{m}) = 0.7$; if there is more foreground veiling, the cloud could have $\tau > 1$ at 7 μm, as our models indeed predict. Another variable is the opacity at 7 μm. Bacmann et al. (2000) assume an opacity that translates to 3.1 cm^2 gm^{-1} of gas, whereas the OH5 dust opacity would imply 12.5 cm^2 gm^{-1}. Bacmann et al. (2000) also find evidence from the density profiles for an outer cut-off radius to the core. Since the core is flattened, this cut-off radius is variable, but taking the geometric mean of the two axes and correcting to a distance of 125 pc yields a radius of 2.6×10^4 AU, similar to our outer radius, but outside the region that we effectively probe. While it is difficult to sort out all of these issues, it seems likely that the discrepancy between our models and those of Bacmann et al. (2000) imply that either they have underestimated the foreground veiling and hence $\tau(7\mu\text{m})$ or we have underestimated the dust temperatures. The new results in the far-infrared are well matched by our low T_d, supporting our interpretation. Because the absorption measurements provide an independent measure of the distribution, this difference leaves a puzzle for further work.

We conclude that Bonnor-Ebert spheres and OH5 dust opacities reproduce the observations of L1689B very well, with $n_c \sim 1 \times 10^6$ cm^{-3}. This density is higher and r_{flat} is smaller than have been found in other studies.

7.2. *L1544*

L1544 is at a distance of 140 pc (Elias 1978). The SCUBA data have slightly better signal to noise than those of L1689B. While the source is clearly elongated (Shirley et al. 2000), we model it as a sphere. Since the radial profiles are spherical averages, this is the most consistent comparison for the present. Ultimately, aspherical models should be constructed, but we address the likely effects in §8. In addition, we model 1300 μm data, subject to the same caveats as for L1689B: in particular, we do not expect to fit the intensity profile at large impact parameters. Magnetic collapse models have been developed for this source (Ciolek & Basu 2000). Using their semi-analytic calculation of dust temperature, Zucconi et al. (2001) find good agreement between this model and the data. Because we focus on spherically averaged data here, we do not attempt to compare this magnetic model to our data.

The results are summarized in Table 3. First, considering only simple Bonnor-Ebert spheres, a model with $n_c = 1 \times 10^6$ cm^{-3} has the lowest χ^2_r for the SCUBA data, as well as the 1300 μm data and the SED. The model with $n_c = 3 \times 10^6$ cm^{-3} has nearly as good a value of $\langle\delta\rangle$, but is slightly worse on the other measures. Density profiles appropriate to non-isothermal Bonnor Ebert spheres fit somewhat worse for $n_c = 1 \times 10^6$ cm^{-3}, but slightly better for $n_c = 1 \times 10^7$ cm^{-3} than their isothermal counterparts.

Most of the models did not include any far-infrared data in the calculation of the SED χ^2_r value. The last two models in Table 3 include the new far-infrared data in the SED χ^2_r value. As with L1689B, the fit is greatly improved with a lower ISRF. The isothermal Bonnor-Ebert model with the ISRF decreased by 0.6 and $n_c = 1 \times 10^6$ cm^{-3} is shown in Figure 6. The spectral index, α, agrees well with the observations.

Because models with very high n_c do not fit the data too badly, we have also considered the extreme limit of a singular sphere ($n_c = \infty$), normalized to have the same density at r_o as the Bonnor-Ebert sphere with $n_c = 1 \times 10^7$ cm^{-3}. This power law model has the density distribution of a singular isothermal sphere at a temperature of 10.4 K (Shu 1977). We considered two models of this type: the first (iPL2) assumed a constant dust temperature of 10 K. This model produced intensity profiles that are too strongly peaked in the inner core, confirming the conclusions of Ward-Thompson, Motte, & André (1999) that power law density distributions *with constant* T_d cannot fit the data. A second model (tPL2) used the radiative transfer code to compute $T_d(r)$ self-consistently. Surprisingly, this model fits the SCUBA data reasonably well. While the fit to the 1300 μm data was clearly worse, our data cannot rule out a simple power law density model *with a self-consistent* $T_d(r)$ for L1544, given the current uncertainties in the data and the modeling. Figure 7 compares the results for the two power law models; it shows how important it is to include the self-consistent $T_d(r)$ in analyzing intensity distributions.

As with L1689B, we compare our results to those obtained from the analysis of 1300 μm emission (Ward-Thompson, Motte, & André 1999) and 7 μm absorption (Bacmann et al. 2000). The assumed distance is the same in all three studies, but (as for L1689B) the opacities differ. Ward-Thompson, Motte, & André (1999) find $n_c = 1 \times 10^6$ cm^{-3} [using the OH5 value of $\kappa_\nu(1300)$], while Bacmann et al. (2000) find $n_c = 4 \times 10^5$, or 1×10^5 if OH5 opacities are correct at 7 μm. The radius of the flat-density-profile inner core ranges from 0 to 1600 AU in our models, compared to 2500 AU (Ward-Thompson, Motte, & André 1999) or 2900 AU (Bacmann et al. 2000). The latter authors also identify an outer (cut-off) radius of 8900 AU. This is close to the size where our chopping and source

asphericity makes it difficult to constrain the density distribution. As with L1689B, our results are qualitatively similar to other analyses, but differ quantitatively; the differences suggest either that we have underestimated T_d or that the optical depth at 7 μm has been underestimated.

As for L1689B, Bonnor-Ebert spheres and OH5 dust fit the data well. Our most striking conclusion that is different from the other studies is that our data *do not* rule out a singular power-law density distribution.

7.3. *L1512*

L1512 is also at a distance of 140 pc, but the submillimeter emission is much weaker than from L1544. While the observational constraints are clearly much weaker than for the other sources, it is interesting to model L1512 because it seems to have a flatter distribution of intensity than the other sources. Shirley et al. (2000) presented only the 850 μm data, but the 450 μm data does have a definable intensity distribution. Both the 450 μm and the 850 μm data and some photometry constrain the models. The photometry was collected in tables in Shirley et al. (2000), except for a datum at 1300 μm from Ward-Thompson, Motte, & André (1999).

The results for L1512 are given in Table 4. For this source we have only considered simple Bonnor-Ebert density distributions — the poor data quality precludes the consideration of more sophisticated models. The best fit is for $n_c = 1 \times 10^5$ cm^{-3}, with $n_c = 3 \times 10^4$ cm^{-3} also acceptable. L1512 is clearly less centrally condensed than the other cores.

The last two models in Table 4 include the new far-infrared data in the SED χ^2_r value. The fit is clearly very bad for the full ISRF; the fit is much improved for an ISRF decreased by 0.3, but it is still worse than for L1689B and L1544. The last model is shown in Fig. 8.

The problem with the SED is that the model fluxes are all higher than the observed values. However, good fits are obtained for the intensity profiles and the spectral index is consistent with the observations. Models with lower n_c fit the lower fluxes better, but do not fit the intensity distribution. If the dust opacities are the same as in the other sources, fitting to the SED requires the core to be less massive. Bonnor-Ebert spheres calculated with $T_K = 5$ K contain less mass, and a model with $n_c = 3 \times 10^4$ cm^{-3} fits both the SCUBA data and the SED best (Table 4). However, such models are hard to justify on physical grounds; the radiative transport calculation produces $T_d(r) > 12$ K everywhere (a model with $T_K = 15$ K fits the SED very poorly). While the density is too low to require $T_K = T_d$, one would have to invoke unusually low gas heating to produce $T_K = 5$ K. Another way to decrease the emission from the model cloud is to use different dust opacities; values between those of OH5 and uncoagulated grains [e.g., column 1 of Ossenkopf & Henning (1994)] would give about the right amount of emission. Such grains are plausible; if L1512 is a younger source, it will have spent less time at densities that are sufficiently high for grain coagulation to occur.

L1512 was detected at 1300 μm by Ward-Thompson, Motte, & André (1999) but was too weak to map. It was also included in the absorption study by Bacmann et al. (2000), but the absorption was too weak to analyze. These results are consistent with our finding that the mass and central density are less than in L1689B and L1544.

The radial profiles of L1512 can be matched if the source is a Bonnor-Ebert sphere with a central density smaller than those of L1689B and L1544.

8. CAVEATS AND FUTURE WORK

The fact that the masses of Bonnor-Ebert spheres, together with the OH5 dust opacities (Ossenkopf & Henning 1994) match the submillimeter fluxes so well suggests that both the physical and dust models may be reasonable. However, the opacity and mass effectively enter as a product; consequently, other mass and opacity combinations cannot be ruled out.

Another caveat is that our models are one-dimensional. Some of the cores (L1544 most notably) are clearly aspherical and (at least) two-dimensional radiative transfer models should be used to interpret the data. We can get a crude estimate of the effect of asphericity on the temperature distribution. Comparing $T_d(r)$ for models with the same n_c but a factor of 2 smaller r_o simulates the effects on heating of having one dimension smaller than the other. In fact, the differences are very small except near the surface of the cloud (≤ 0.2 K, or 3%, for $r \leq 1 \times 10^4$ AU). Semi-analytic calculations of T_d in a two-dimensional geometry (Zucconi et al. 2001) find modest differences in the $T_d(r)$ along long and short axes.

Differences in the assumed density law will produce different $T_d(r)$ in general, as can be seen from Fig. 4. However, if one plots the T_d versus column density, the behavior is much more universal, as would be expected. This is shown in Fig. 9 for a variety of density profiles. The curves of $T_d(r)$ track each other until they approach their maximum value, where geometrical effects near the center of the cloud cause them to deviate from models with higher total column density. This figure may be useful for those modeling different density distributions who do not have access to a radiative transport code. For example, the $T_d \sim 10$ K computed from gray-body fits to the SED (Ward-Thompson et al. 2001) for L1689B and L1544 would correspond to the model T_d at about 1/3 the total column density into the cloud; in contrast, the radius at which $T_d = 10$ K is about 4×10^3 AU (Figs. 5 and 6), about 0.13 of the outer radius, enclosing 0.15 of the total mass. Clearly, gray-body fits to a constant T_d weight radius, column density, and mass differently, depending on the detailed density and temperature distributions.

Local variations in the ISRF are another source of uncertainty. If local sources increase the strength of the ISRF, T_d will increase. However, in practice, large changes in the ISRF strength are needed for significant variations to occur. Approximately, $T_d \propto L^{1/(\beta+4)}$, where L is the ISRF luminosity and β is the power-law index for the opacity ($\kappa_\nu \propto \nu^\beta$) (Doty & Leung 1994). For typical values of β, the exponent is only 0.2 to 0.25, so that doubling the ISRF strength will increase the dust temperature by just 15-20%. Full radiative transfer models run with higher ISRF strengths confirm this simple analysis. Figure 3 shows the $T_d(r)$ calculated for the same physical model, but with the Black-Draine ISRF multiplied by a factor of 2 (except for the cosmic background radiation). The temperatures are higher at all radii by a factor around 1.14, as would be

predicted by the simple relations above.

In fact, the new far-infrared data indicate a lower ISRF than we have assumed, even for L1689B, where the ISRF is generally considered to be enhanced. Thus lower T_d are more likely than higher. Since Ward-Thompson et al. (2001) describe their results in terms of *enhanced* ISRF, a word of explanation is in order. They use the ISRF of Mathis, Mezger, & Panagia (1983), which is considerably lower than the Black-Draine field that we use (cf. Fig. 2a) in the mid-infrared to far-infrared region where they constrain the field. It seems that, for these cores at least, the correct value lies between the two standard choices for the ISRF. The far-infrared data strongly constrain the ISRF because they are exponentially sensitive to T_d in this regime; future measurements and modeling will allow much better knowledge of the local ISRF.

9. CONCLUSIONS

We have modeled the emission from dust in pre-protostellar cores, including a self-consistent calculation of the temperature distribution ($T_d(r)$) for an input density distribution. We have also simulated the observations by convolving models with the observed beam and applying chopping to the models. Using the calculated $T_d(r)$ has a substantial impact on the conclusions. Compared to earlier studies that assumed a constant $T_d(r)$, our models indicate smaller regions of relatively constant density (by factors of 0.5 to 0.9) and higher central densities (by factors of 3 to 10). Indeed, for L1544, a singular, power-law density distribution cannot be ruled out.

For the three sources we have modeled, there seems to be a sequence of increasing central condensation, from L1512 to L1689B to L1544. While many more starless cores need to be modeled, it is possible that a new sequence of cores may be identified, in which increasing central condensation is the primary variable. The denser two of these cores, L1689B and L1544, have spectroscopic evidence of contraction motions (Tafalla et al. 1998; Gregersen & Evans 2000), while L1512 does not (Gregersen & Evans 2000), consistent with this suggested sequence.

It is interesting that Bonnor-Ebert spheres fit the data well, even though unstable spheres are needed in all cases. Magnetic fields may allow these nominally unstable objects to persist, but in the absence of a suitable 2D/3D radiative transfer model we are not able to say whether or not the existing ambipolar diffusion controlled collapse models are consistent with the observations.

Johnstone et al. (2000) have also used Bonnor-Ebert spheres to fit their SCUBA data in the ρ Ophiuchus molecular cloud. They find smaller outer radii and smaller degrees of central condensation, but they have used models with constant $T_d = T_K$. The smaller outer radii may reflect the crowded conditions and higher ambient pressures in the ρ Ophiuchus region, compared to the "elbow room" available to the isolated cores in this study. More detailed analysis of the clustered regions, including calculations of $T_d(r)$, and more extensive studies of isolated regions will together delineate the differences in initial conditions for clustered and isolated star formation.

We are grateful to the referee, C. Wilson, for helpful suggestions and to G. Ciolek and S. Basu for discussion of magnetic models. We are very grateful to P. André and D. Ward-Thompson, who provided data and helpful discussion. We thank E. van Dishoeck for advice on the interstellar radiation field and M. Greenberg for helpful discussion on alternative grain heating mechanisms. T. Greathouse helped with some of the computer codes. The JCMT is operated by the Joint Astronomy Centre on behalf of the Particle Physics and Astronomy Research Council of the United Kingdom, The Netherlands Organization for Scientific Research and the National Research Council of Canada. We thank the State of Texas and NASA (Grant NAG5-7203) for support. NJE thanks the Fulbright Program and PPARC for support while at University College London and the Netherlands Organization for Scientific Research (NWO) bezoekersbeurs grant and NOVA for support at Leiden Observatory.

REFERENCES

Adams, F. C., Lada, C. J., and Shu, F. H. 1987, ApJ, 312, 788
André, P., Ward-Thompson, D., and Barsony, M. 1993, ApJ, 406, 122
André, P., Ward-Thompson, D. and Barsony, M. 2000, Protostars and Planets IV (Book - Tucson: University of Arizona Press; eds Mannings, V., Boss, A.P., Russell, S. S.), p. 59 , 59
André, P., Ward-Thompson, D. and Motte, F. 1996, A&A, 314, 625
Bacmann, A., André, P., Puget, J.-L., Abergel, A., Bontemps, S., & Ward-Thompson, D. 2000, A&A, 361, 555
Benson, P. J., & Myers, P. C. 1989, ApJS, 71, 89
Black, J. H. 1994, ASP Conf. Ser. 58: The First Symposium on the Infrared Cirrus and Diffuse Interstellar Clouds, 355
de Boisanger, C., Helmich, F. P. & van Dishoeck, E. F. 1996, A&A, 310, 315
Bonnor, W.B. 1956, MNRAS, 116, 351
Caselli, P., Walmsley, C. M., Terzieva, R. & Herbst, E. 1998, ApJ, 499, 234
Cecchi-Pestellini, C. & Aiello, S. 1992, MNRAS, 258, 125
Ciolek, G.E. & Basu, S. 2000, ApJ, 529, 925
Ciolek, G. E. & Basu, S. 2001, ApJ, 547, 272
Ciolek, G.E. & Mouschovias, T. Ch. 1994, ApJ, 425, 142
de Geus, E. J., de Zeeuw, P. T., & Lub, J. 1989, A&A, 216, 44
de Zeeuw, P. T., Hoogerwerf, R., de Bruijne, J. H. J., Brown, A. G. A. and Blaauw, A. 1999, AJ, 117, 354
Doty, S. D. and Leung, C. M. 1994, ApJ, 424, 729
Doty, S. D. and Neufeld, D. A. 1997, ApJ, 489, 122
Draine, B. T. 1978, ApJS, 36, 595
Ebert, R. 1955, *Zs. Ap.*, 217
Egan, M. P., Leung, C. M., & Spagna, G. R., 1988, Comput. Phys. Comm., 48, 271
Elias, J. H. 1978, ApJ, 224, 857
Foster, P. N. & Chevalier, R. A. 1993, ApJ, 416, 303
Goldsmith, P. F. 2001, ApJ, submitted
Goldsmith, P. F. & Langer, W. D. 1978, ApJ, 222, 881
Gredel, R., Lepp, S., Dalgarno, A. & Herbst, E. 1989, ApJ, 347, 289
Greenberg, J. M. 1991, NATO Advanced Science Institutes (ASI) Series C: Mathematical and Physical Sciences, Proceedings of the NATO Advanced Study Institute on Chemistry in Space, Erice, Italy, May 10-20, 1989, J. M. Greenberg and V. Pirronello, Dordrecht: Kluwer, 227
Greenberg, J. M. & Li, A. 1996, New Extragalactic Perspectives in the New South Africa, D. L. Block and J. M. Greenberg, Dordrecht: Kluwer, 118
Gregersen, E. M. and Evans, N. J. 2000, ApJ, 538, 260
Henriksen, R., André, P. and Bontemps, S. 1997, A&A, 323, 549
Johnstone, D., Wilson, C. D., Moriarty-Schieven, G., Joncas, G., Smith, G., Gregersen, E., & Fich, M. 2000, ApJ, 545, 327
Knude, J. and Hog, E. 1998, A&A, 338, 897
Lada, C. J. 1987, in IAU Symp. 115, Star Formation Regions, ed. M Peimbert & J. Jugaku (Dordrecht:Reidel), 1
Leung, C. M. 1975, ApJ, 199, 340
Mathis, J. S., Mezger, P. G. & Panagia, N. 1983, A&A, 128, 212
McLaughlin, D. E. & Pudritz, R. E. 1997, ApJ, 476, 750
Myers, P. C., & Benson, P. J. 1983, ApJ, 266 309
Ossenkopf, V. and Henning, T. 1994, A&A, 291, 943
Prasad, S. S. & Tarafdar, S. P. 1983, ApJ, 267, 603

Shirley, Y. L., Evans, N. J., II, Rawlings, J. M. C., & Gregersen, E. M. 2000 ApJS, 131, 249
Shu, F. H. 1977, ApJ, 214, 488
Tafalla, M., Mardones, D., Myers, P. C., Caselli, P., Bachiller, R. and Benson, P. J. 1998, ApJ, 504, 900
Takahashi, T., Silk, J., & Hollenbach, D. J. 1983, ApJ, 275, 145
van der Tak, F. F. S. & van Dishoeck, E. F. 2000, A&A, 358, L79
van der Tak, F. F. S., van Dishoeck, E. F., Evans, N. J., Bakker, E. J. and Blake, G. A. 1999, ApJ, 522, 991
van der Tak, F. F. S., van Dishoeck, E. F., Evans, N. J., II, & Blake, G. A. 2000, ApJ, 537, 283
van Dishoeck, E. F. 1988, Rate Coefficients in Astrochemistry, T. L. Millar and D. A. Williams, Dordrect: Kluwer, 49
Ward-Thompson, D. & André, P. 1999, The Universe as Seen by ISO. Eds. P. Cox & M. F. Kessler. ESA-SP 427. 427, 463
Ward-Thompson, D., André, P., & Kirk, J. M. 2001, MNRAS, submitted.
Ward-Thompson, D., André, P. and Motte, F. 1998, ASP Conf. Ser. 132: Star Formation with the Infrared Space Observatory, 195
Ward-Thompson, D., Motte, F. and André, P. 1999, MNRAS, 305, 143
Ward-Thompson, D., Scott, P. F., Hills, R. E. and André, P. 1994, MNRAS, 268, 276
Webber, W. R. 1998, ApJ, 506, 329
Zhou, S., Evans, N. J., Butner, H. M., Kutner, M. L., Leung, C. M. and Mundy, L. G. 1990, ApJ, 363, 168
Zucconi, A., Walsmley, C. M., and Galli, D. 2001, A&A, submitted

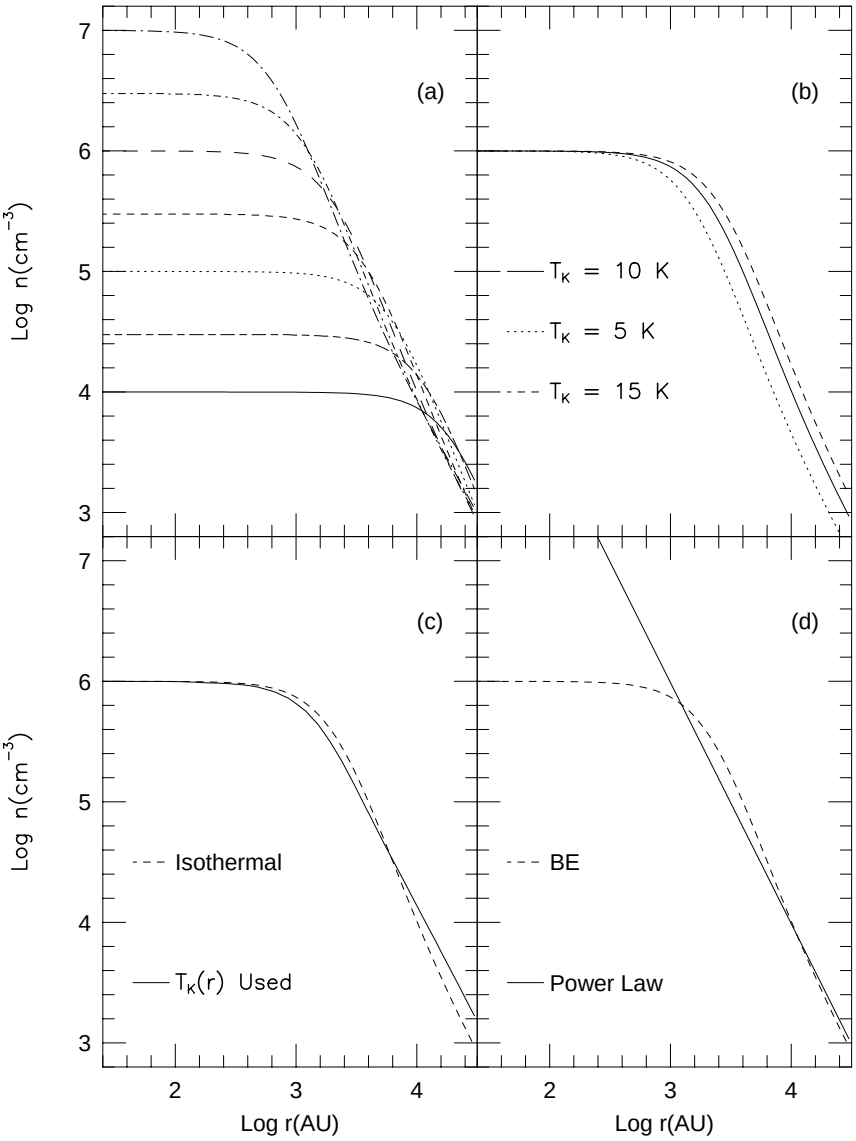

FIG. 1.— Plots of log density versus log radius in AU for the input physical models. In (a), Bonnor-Ebert spheres with constant kinetic temperature, $T_K = 10$ K and central densities from $n_c = 1 \times 10^4$ to $n_c = 1 \times 10^7$ cm^{-3} are shown. In (b), Bonnor-Ebert spheres with $n_c = 1 \times 10^6$ cm^{-3} are shown for different, constant kinetic temperatures. In (c), a Bonnor-Ebert sphere with a variation in T_K, based on iteration with the radiative transport code, and assuming $T_K(r) = T_d(r)$, is compared to an isothermal ($T_K = 10$ K) Bonnor-Ebert sphere, with the same n_c. In (d), a power law (PL2) corresponding to a singular isothermal sphere with $T_K = 10.4$ is compared to a Bonnor-Ebert sphere with $n_c = 1 \times 10^6$ cm^{-3}.

TABLE 1
PHYSICAL MODELS

No.	Type[a]	r_o[b] (AU)	n_c[c] (cm^{-3})	T_K[d] (K)	r_{flat}[e] (AU)	n_o[f] (cm^{-3})	M[g] ($M_\odot$)
1	BE	3×10^4	1×10^4	10	16200	1.84×10^3	2.63
2	BE	3×10^4	3×10^4	10	9300	1.57×10^3	3.15
3	BE	3×10^4	1×10^5	10	5110	1.17×10^3	3.06
4	BE	3×10^4	3×10^5	10	2990	9.79×10^2	2.75
5	BE	3×10^4	1×10^6	10	1600	9.38×10^2	2.46
6	BE	3×10^4	3×10^6	10	930	9.90×10^2	2.34
7	BE	3×10^4	1×10^7	10	500	1.09×10^3	2.34
8	BE	6×10^4	3×10^5	10	2990	2.34×10^2	4.86
9	BE	1.5×10^4	1×10^6	10	1600	3.98×10^3	1.40
10	BE	6×10^4	1×10^6	10	1600	2.50×10^2	4.64
11	BE	6×10^4	3×10^6	10	930	2.74×10^2	4.69
12	BE	3×10^4	3×10^4	5	6590	6.59×10^2	1.58
13	BE	3×10^4	1×10^5	5	3600	5.14×10^2	1.43
14	BE	3×10^4	1×10^6	5	1130	4.82×10^2	1.18
15	BE	3×10^4	1×10^6	15	1970	1.41×10^3	3.82
16	tBE[4]	3×10^4	3×10^5	~7-15	2500	1.68×10^3	3.55
17	tBE[5]	3×10^4	1×10^6	~7-15	1300	1.68×10^3	3.42
18	tBE[10]	6×10^4	1×10^6	~7-15	1300	4.27×10^2	7.25
19	tBE[7]	3×10^4	1×10^7	~7-15	400	1.77×10^3	3.44
20	iPL2	3×10^4	1.56×10^9	10.4	...	1.08×10^3	2.06
21	tPL2	3×10^4	1.56×10^9	10.4	...	1.08×10^3	2.06

[a] BE is an isothermal Bonnor-Ebert sphere; tBE is a Bonnor-Ebert sphere with a temperature gradient; iPL2 is a power law, with an exponent of 2 and constant dust temperature of 10 K; tPL2 is the same power law with a dust temperature calculated by the radiative transport code.
[b] The outer radius is r_o.
[c] n_c is the central density, at $r = r_i$.
[d] T_K is the gas kinetic temperature used to compute the density distribution.
[e] r_{flat} is the radius where the density drops to half the central density (n_c).
[f] n_o is the density at the outer radius.
[g] M is the mass enclosed within r_o.

TABLE 2
MODELS OF L1689B

No.[a]	Type	n_c (cm^{-3})	M ($M_\odot$)	χ^2_r SCUBA	$\langle\delta\rangle$ SCUBA	χ^2_r 1300[b]	χ^2_r SED	Comments
3	BE	1×10^5	3.06	16	0.83	1036–1560	18	
4	BE	3×10^5	2.75	2.4	0.38	338–577	17	
5	BE	1×10^6	2.46	1.4	0.26	26–102	16	
6	BE	3×10^6	2.34	5.1	0.51	30–22	14	
7	BE	1×10^7	2.34	8.0	0.73	104–48	11	
9	BE	1×10^6	1.40	1.2	0.26	27–58	6.6	$r_o = 1.5\times10^4$
8	BE	1×10^6	4.86	1.3	0.26	26–128	18	$r_o = 6\times10^4$, $r_i = 50$
5	BE	1×10^6	2.46	1.4	0.26	25–102	16	$r_i = 50$
16	tBE	3×10^5	3.55	3.3	0.38	333–735	20	
17	tBE	1×10^6	3.42	1.3	0.26	41–235	19	
19	tBE	1×10^7	3.44	4.1	0.52	43–82	16	
4	BE	3×10^5	2.75	3.1	0.45	375–635	212	OH2 Dust
5	BE	1×10^6	2.46	1.0	0.27	39–131	237	OH2 Dust
5	BE	1×10^6	2.46	1.4	0.26	26–102	14[c]	ISRF ×1
5	BE	1×10^6	2.46	1.1	0.27	31–123	1.5[c]	ISRF ×0.5

[a]The model numbers refer to the physical model in Table 1.
[b]The first value is for chopping by 120″; the second is for no chopping.
[c]Only these two models include the new far-infrared data in the calculation of χ^2_r; the other models included previous far-infrared data.

TABLE 3
MODELS OF L1544

No.[a]	Type	n_c (cm^{-3})	M ($M_\odot$)	χ^2_r SCUBA	$\langle\delta\rangle$ SCUBA	χ^2_r 1300[b]	χ^2_r SED	Comments
4	BE	3×10^5	2.75	18	0.63	123–198	2.1	
5	BE	1×10^6	2.46	0.73	0.17	14–26	1.0	
6	BE	3×10^6	2.34	3.0	0.19	118–49	1.2	
7	BE	1×10^7	2.34	7.3	0.39	258–114	2.0	
17	tBE	1×10^6	3.42	2.8	0.22	28–88	2.6	
19	tBE	1×10^7	3.44	2.0	0.24	160–88	2.0	
20	iPL2	···	2.06	22	0.95	480-247	11	
21	tPL2	···	2.06	3.0	0.27	149–210	3.6	
5	BE	1×10^6	2.46	0.73	0.17	14–26	7.2[c]	IRSF ×1
5	BE	1×10^6	2.46	1.1	0.22	13–31	2.8[c]	IRSF ×0.6

[a]The model numbers refer to the physical model in Table 1.
[b]The first value is for chopping by 120″; the second is for no chopping.
[c]Only these two models include the far-infrared data in the calculation of χ^2_r.

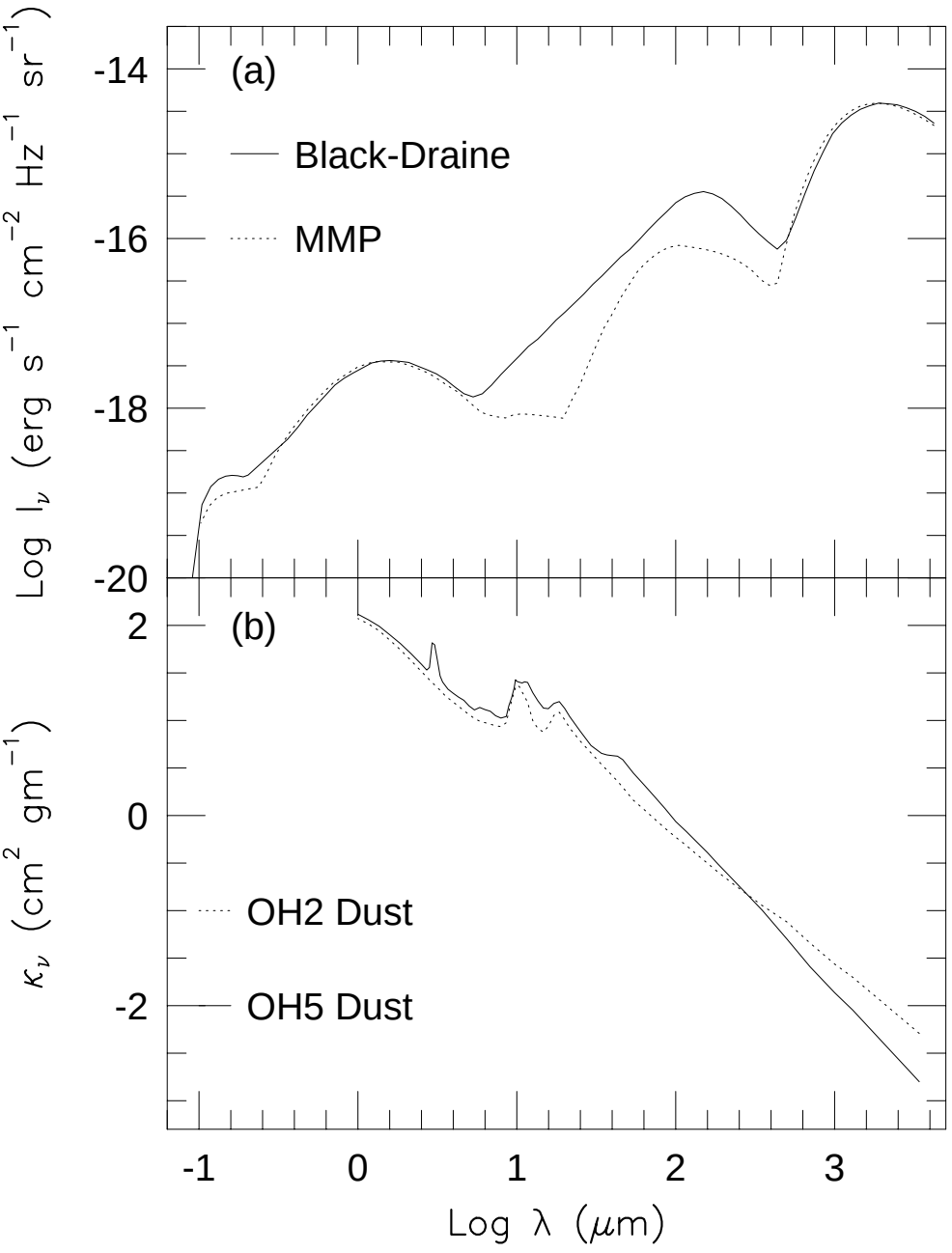

FIG. 2.— In (a), the interstellar radiation field used in previous versions of the code ("MMP") is compared with that used here (Black-Draine). "MMP" is close to the ISRF used by Mathis, Mezger, & Panagia (1983), supplemented by a blackbody for the cosmic background radiation. The ISRF labeled Black-Draine uses the curve in Black (1994) for $\lambda \geq 0.36$ μm, and Draine (1978) for $\lambda < 0.36$ μm. In (b), the opacity per gram of gas (κ_ν) for OH5 and OH2 dust, based on Ossenkopf & Henning (1994) and a gas to dust mass ratio of 100, is plotted versus wavelength.

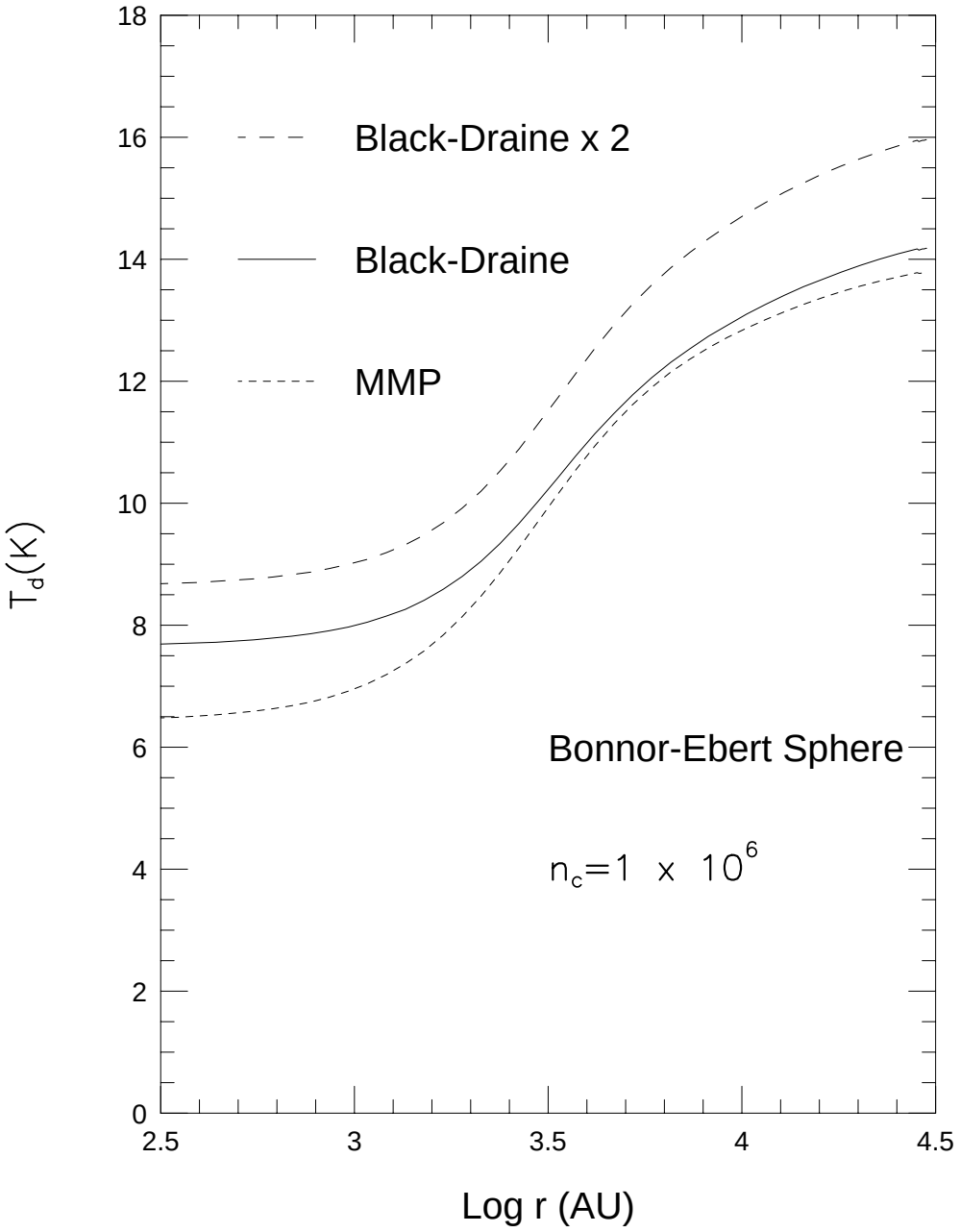

FIG. 3.— Shows the effects on the dust temperature distribution of changing the ISRF from "MMP" to Black-Draine, and of using twice the average ISRF. A Bonnor-Ebert sphere with $n_c = 1 \times 10^6$ cm^{-3} and $T_K = 10$ K was used for all three calculations.

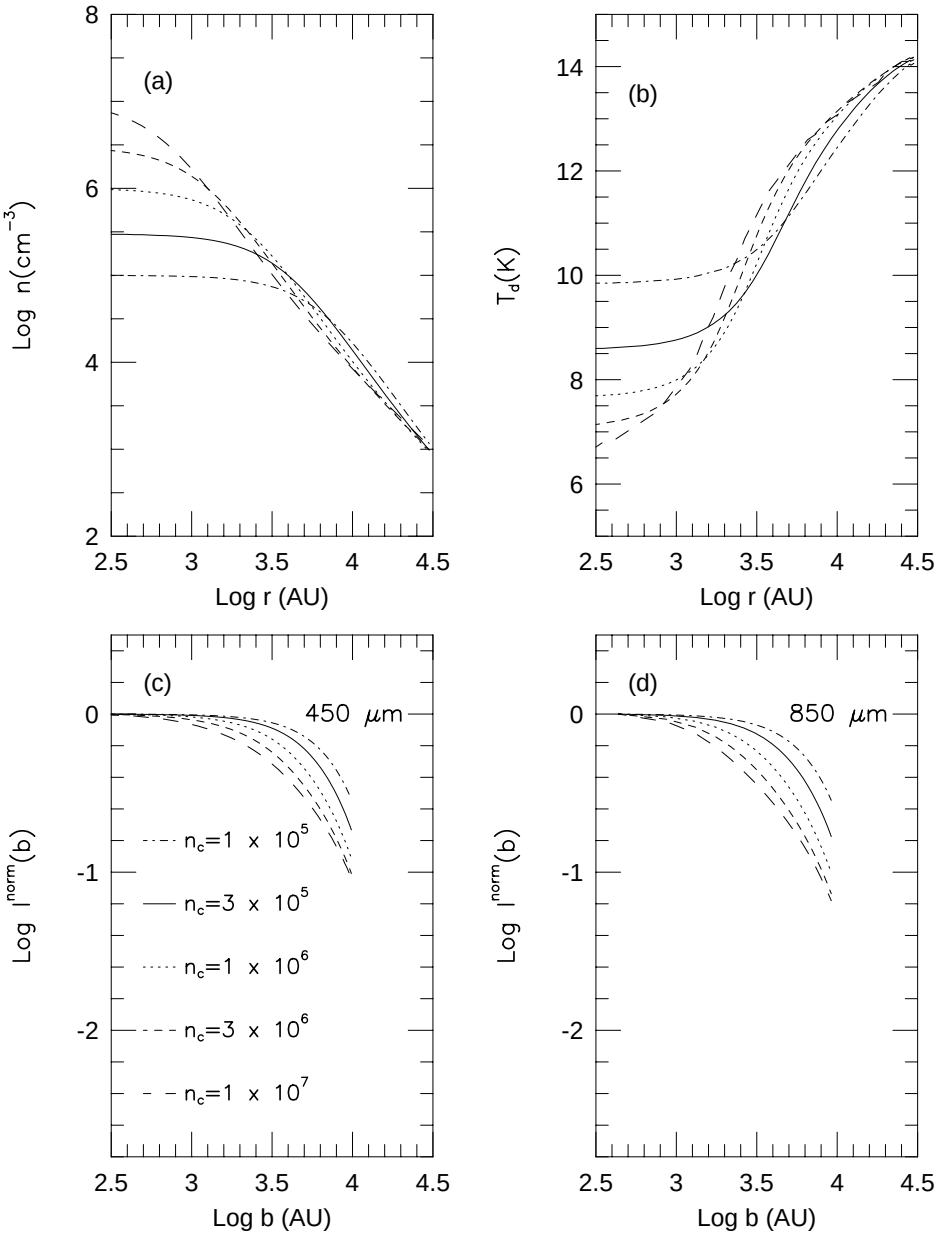

FIG. 4.— The density distributions for a series of Bonner-Ebert spheres are shown in (a). The resulting temperature distributions are shown in (b), with the same line coding; the densest models have the lowest central temperatures. In (c), the resulting intensity distributions at 450 μm are shown. In (d), the results for 850 μm are shown. The same line coding is used for all panels, with the densest models showing the fastest fall-off with radius. The model emission in panels c and d has been convolved with the observed beam and chopping by $120''$ has been simulated, causing some of the drop around impact parameter, $b \sim 10,000$ AU, for a distance of 125 pc.

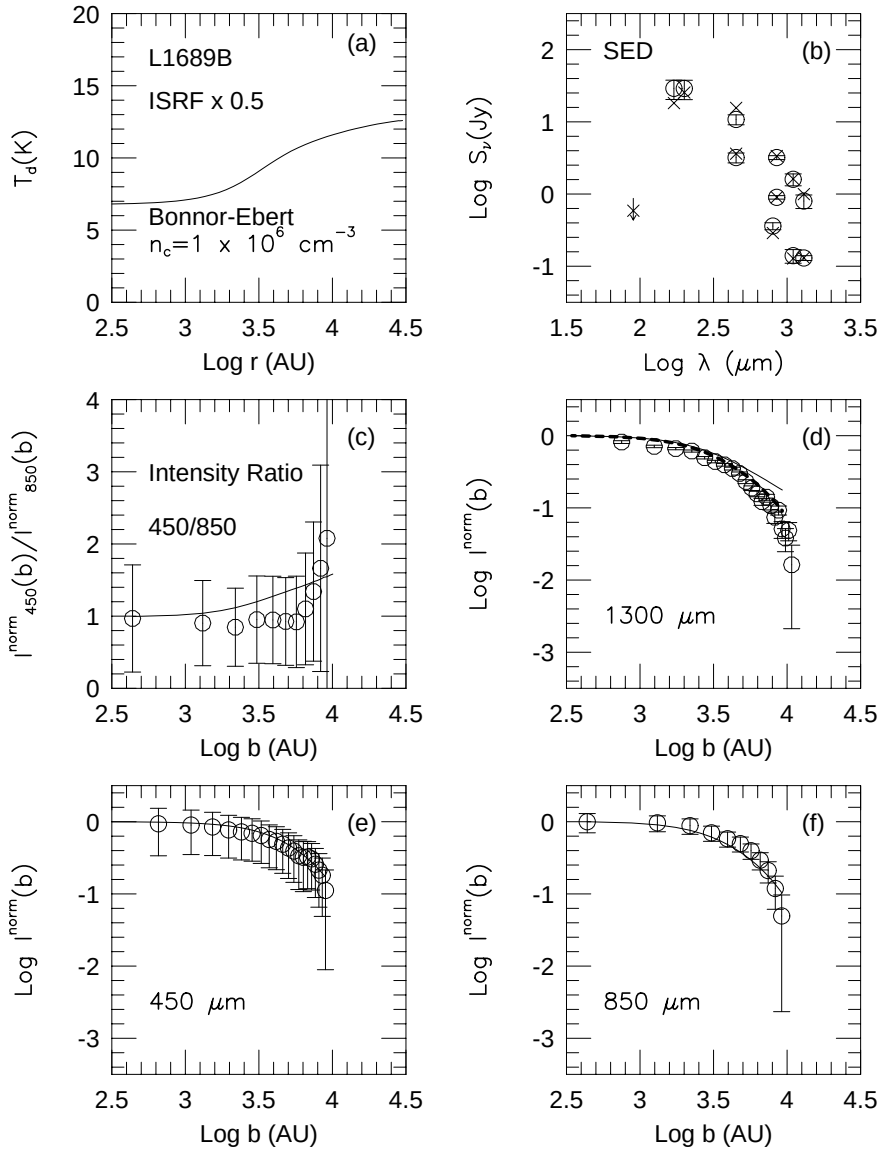

FIG. 5.— A model for L1689B that fits the data well, a Bonnor-Ebert sphere with $n_c = 1 \times 10^6$ cm^{-3} and a Black-Draine ISRF multiplied by 0.5. The temperature distribution is shown in (a). The observed SED is shown in (b) as circles with errorbars and an upper limit at 90 μm; multiple values at the same wavelength are data with different beams. The crosses are the model predictions for the same beams. The bottom two panels, (e) and (f), show for 450 and 850 μm, the observed, normalized intensity profile (circles and error bars) and the model (solid line), with simulated chopping. Panel (d) shows the data at 1300 μm of André, Ward-Thompson, & Motte (1996) and the model without simulated chopping (solid line) and with a simulation of chopping by 120″ (heavy dashed line). Panel (c) shows the ratio of the 450 and 850 μm normalized intensities with the same conventions. Note that normalization constrains the value to unity at the innermost point. At 125 pc, $b = 10^4$ AU corresponds to 80″.

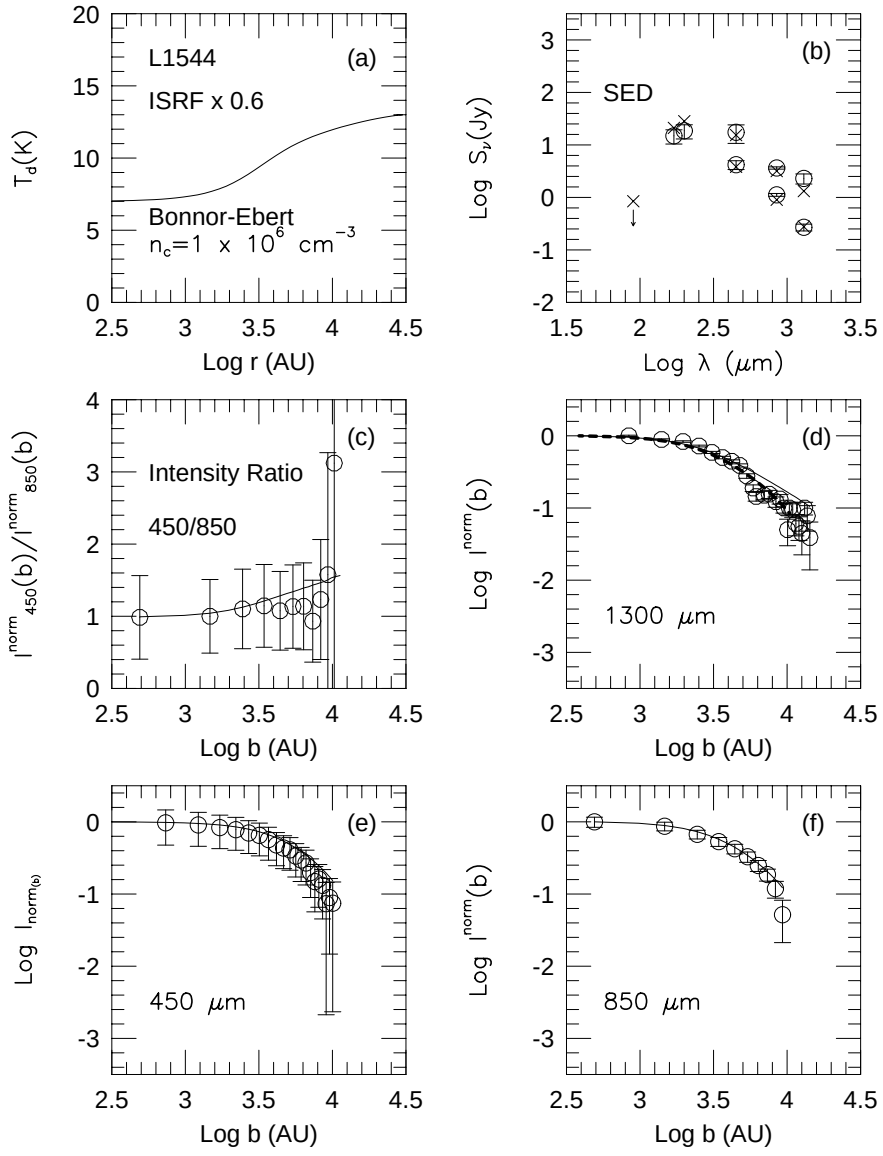

FIG. 6.— The same as Fig. 5, but for L1544. The model is a Bonnor-Ebert sphere with $n_c = 1 \times 10^6$ cm^{-3} and a Black-Draine ISRF multiplied by 0.6. The 1300 μm data is from Ward-Thompson, Motte, & André (1999). At 140 pc, $b = 10^4$ AU corresponds to 71″.

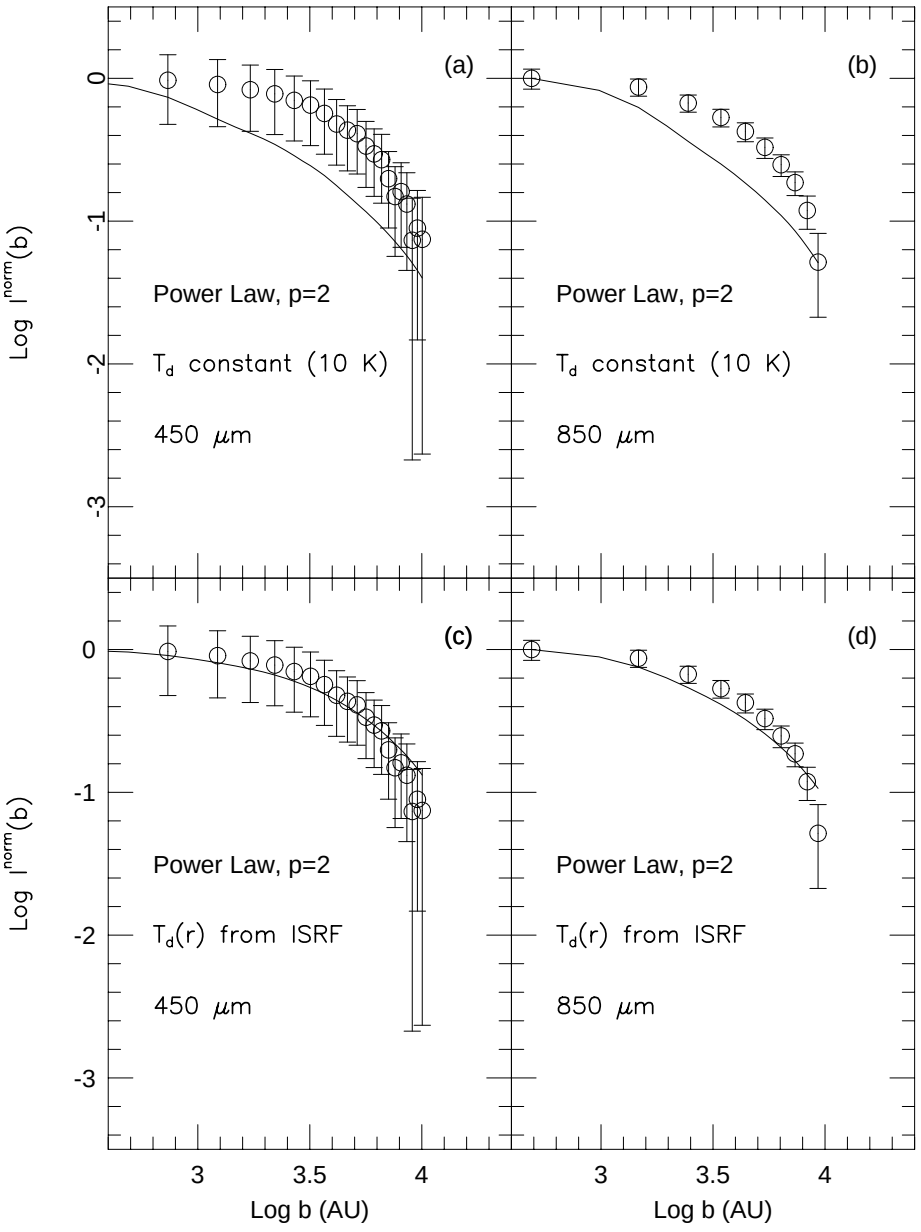

FIG. 7.— The normalized intensity distributions at 450 (a and c) and 850 (b and d) μm for a power law density distribution, $n(r) = n(r_o)(r/r_o)^{-p}$, with $n(r_o) = 1.02 \times 10^3$, $p = 2$, and $r_o = 3 \times 10^4$ AU. The observations are of L1544. The top panels (a and b) show the model predictions with a constant $T_d(r) = 10$ K, while the bottom panels (c and d) show predictions for $T_d(r)$ calculated self-consistently with the radiative transport code, using the full Black-Draine ISRF.

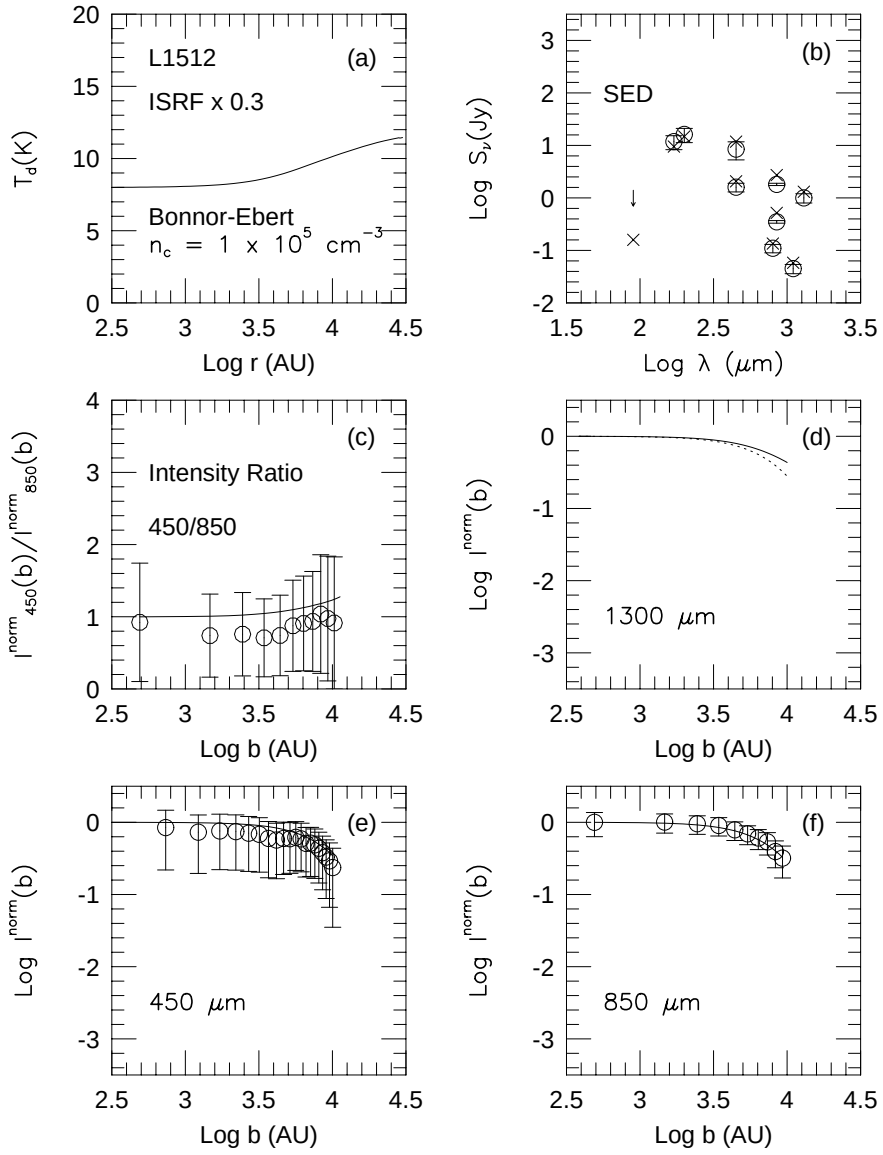

FIG. 8.— The same as Fig. 5, but for L1512. The model is a Bonnor-Ebert sphere with $n_c = 1 \times 10^5$ cm^{-3} and a Black-Draine ISRF multiplied by 0.3. No data exist at 1300 μm, so only the model predictions are shown (solid line for no chopping, dashed line for chopping by 120″). At 140 pc, $b = 10^4$ AU corresponds to 71″.

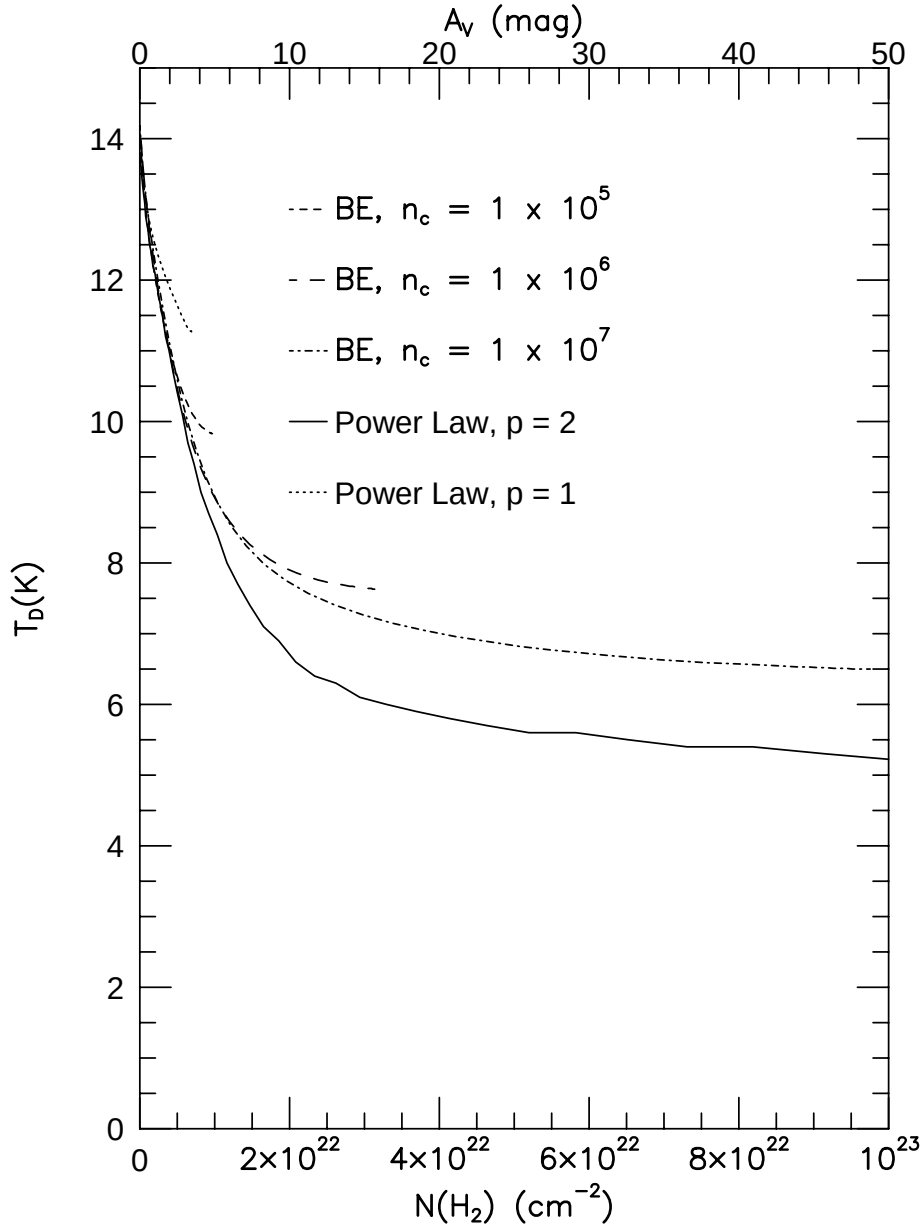

FIG. 9.— The dust temperature is plotted versus gas column density for a variety of models. The visual extinction is marked on the top axis, using standard conversions. The calculation was done for the full Black-Draine ISRF.

TABLE 4
MODELS OF L1512

No.[a]	Type	n_c (cm^{-3})	M ($M_\odot$)	χ^2_r SCUBA	$\langle\delta\rangle$ SCUBA	χ^2_r SED	Comments
1	BE	1×10^4	2.63	3.2	0.93	6.6	
2	BE	3×10^4	3.15	1.1	0.62	62	
3	BE	1×10^5	3.06	0.38	0.41	179	
4	BE	3×10^5	2.75	1.6	0.59	276	
12	BE	3×10^4	1.58	0.31	0.37	5.1	$T_K = 5$
13	BE	1×10^5	1.43	1.4	0.57	30	$T_K = 5$
14	BE	1×10^6	1.18	7.7	1.2	65	$T_K = 5$
15	BE	1×10^6	3.82	3.1	0.73	666	$T_K = 15$
3	BE	1×10^5	3.06	0.38	0.41	155[b]	ISRF $\times 1$
3	BE	1×10^5	3.06	0.41	0.43	20[b]	ISRF $\times 0.3$

[a] The model numbers refer to the physical model in Table 1.
[b] Only these two models include the far-infrared data in the calculation of χ^2_r.